International Journal of Heat and Mass Transfer 106 (2017) 731–740

Contents lists available at ScienceDirect

International Journal of Heat and Mass Transfer

journal homepage: www.elsevier.com/locate/ijhmt

Multiscale thermal nonequilibria for record superadiabatic-radiant-burner efficiency: Experiment and analyses

Vahid Vandadi [a,1], Hu Wu [b,1], Oh Chae Kwon [b], Massoud Kaviany [c], Chanwoo Park [d,*]

[a] Department of Mechanical Engineering, University of Nevada, Reno, NV 89557, USA
[b] School of Mechanical Engineering, Sungkyunkwan University, Suwon, Gyeonggi-do 16419, Republic of Korea
[c] Department of Mechanical Engineering, University of Michigan, Ann Arbor, MI 48109, USA
[d] Department of Mechanical and Aerospace Engineering, University of Missouri, Columbia, MO 65211, USA

ARTICLE INFO

Article history:
Received 20 June 2016
Received in revised form 19 September 2016
Accepted 20 September 2016
Available online 13 October 2016

Keywords:
Superadiabatic
Porous burner
Heat recirculation
Preheating
Lean combustion

ABSTRACT

A record radiation efficiency of 37% is achieved using a two-layered porous (SiC foam, fine and course) burner using multiscale thermal nonequilibria and effective heat recirculation. The porous burner holds the flame and heats finned SiC rods effectively conducting heat to radiating disks downstream, while the flue gas is intercepted before leaving the disk spacing by a preheater carrying secondary air that mixes upstream with the fuel and primary air. These result in superadiabatic combustion in porous layers and fuel-gas preheating that causes exiting flue gas having a temperature lower than the radiating disks. These orchestrated heat recirculation and preheating extend the lean flammability to 0.24 equivalence ratio, and allow the flue gas temperature to be over 50 K below the radiating disks temperature. A three-dimensional model of the structures with a two-step combustion reaction allow to predict the combustion and emission and related convection, conduction and radiation heat transfer, with excellent agreement with the experiments over wide ranges of fuel flow rate and equivalence ratio.

1. Introduction

The premixed combustion in porous media often becomes a superadiabatic combustion which is also known as "excess enthalpy" burning caused by an internal heat recirculation [1–12]. The well-known internal heat recirculation in the porous burner consists of interstitial convection, solid conduction, and surface radiation of combustion heat to internally preheat the incoming fuel–air mixture flow. Due to this heat recirculation, the porous burners are capable of burning low-calorific-value fuels (low fuel equivalence ratios) that would not normally be combustible, allowing for the utilization of what would otherwise be wasted energy resources [13]. The internal heat recirculation also makes it possible for the porous burner to operate at higher flame speeds (large energy throughputs) than the laminar flame, greatly reducing emissions and extending combustion stability which is characterized by flame blow-off, flashback or extinction [3,13–15]. In addition to the internal heat recirculation, the heat recovery from exiting exhaust gas using a preheater can further lower the fuel lean limit to as low as 0.1 equivalence ratio with a mixture of methane and hydrogen [10,14,16]. Such an ultra-lean combustion occurring at low temperatures emits less NO_x, unburned hydrocarbon (UHC) and CO [8].

The early design of the porous burners used a single-layered (monolithic) burner made of ceramic foam materials [1,14,17] which was often used to study a non-stationary combustion (filtration combustion). In recent years, multi-layer porous burners have been extensively investigated [2,8,9,16,18,19] due to the unique advantages, e.g., submerged flame, extended flammability limit, lean combustion and low emission. A two-layered porous burner first used by Durst and Trimis [20] can stabilize flame at the interface between the two different porous layers with different distinctive geometrical properties (porosity and pore diameter) over a wide range of flow rate.

In the two-layered porous burner, the first layer (upstream) of the burner has finer (smaller) pores than that of the second layer (downstream). The pore diameter of the finer layer is typically in the order of 500 μm and less than the minimum diameter required for the flame propagation to serve as a flame arrestor, whereas the pore diameter of the coarse layer is about 2 mm with a similar porosity to that of the finer layer [8]. The flame stabilization (blow-off, flashback or extinction) near the interface is greatly affected by the rapid changes in gas velocity and heat recirculation across the interface of the porous layers [13,15].

* Corresponding author at: Department of Mechanical and Aerospace Engineering, University of Missouri, Columbia, E3423 Lafferre Hall, Columbia, MO 65211, USA.
E-mail address: parkchanw@missouri.edu (C. Park).
[1] Equal contributions to this article.

http://dx.doi.org/10.1016/j.ijheatmasstransfer.2016.09.067
0017-9310/

Nomenclature

A	pre-exponential factor of combustion reaction [1/s]
c_p	specific heat [J/kg-K]
C_j	molar concentration of species j [kmol/m^3]
D_p	pore diameter [m]
E_a	activation energy [J/kmol]
h_{gs}	interstitial heat transfer coefficient [W/m^2-K]
k	thermal conductivity [W/m-K]
k_r	rate constant
L	length [m]
M_w	molecular weight [kg/kmol]
$\mathrm{Nu}_{D,p}$	Nusselt number
N_R	number of reactions
P	pressure [Pa]
Q	heat rate [W]
R	reaction rate [kg/m^3-s]
Re	Reynolds number, $\rho_g \varepsilon u_g D_p/\mu$
R_g	universal gas constant [J/kmol-K]
$\dot{S}_{r,c}$	rate of heat generation [W/m^3]
T	temperature [K]
u	velocity [m/s]
x	coordinate [m]

Greek letters

β	temperature exponent
ΔH_r	heat of reaction [W/kg]
ε	porosity
ε_r	emissivity
η	exponent
η_r	radiation efficiency
μ	dynamic viscosity [Pa-s]
υ	stoichiometric coefficient
ρ	density [kg/m^3]
σ_e	extinction coefficient [1/m]
σ_{SB}	Stefan-Boltzmann constant [W/m^2-K^4]
ϕ	equivalence ratio

Subscripts

1,2	indices
a	activation
amb	ambient
exh	exhaust
F	fuel or flame
g	gas phase
gs	gas to solid
i, j	index
k	conduction
p	pore or particle
ph	preheater
r	radiation or reaction
s	solid phase
sr	radiating surface
stoich	stoichiometric
t	target
u	advection

Superscripts

m	exponent or coefficient

The modeling of the lean premixed combustion in porous media employs a local volume-averaged formulation [5,10,29] and direct simulation [4] based on either thermal equilibrium or using nonequilibrium treatment. The interstitial heat transfer inside the small-scale pores of the porous media plays a significant role in heat recirculation in porous burners [5,8,21]. The volume-averaged model could not predict the minimum sustainable flame speeds in the burner (flashback limit) and the model predictions of flame speed increasingly deviated from experimental results as the equivalence ratio approached stoichiometric because no turbulence or flame-stretching effects in the small-scale porous structures were considered [22].

Despite the notable progress in the field of porous burners, as presented in a detailed review on the various designs of porous burners by Wood and Harris [13], the combustion of lean mixtures of fuel and air, remains relatively unexplored. One of the main topics that have not been fully explored is the effect of the use of supplementary external preheating of the incoming fuel/air mixture [13]. Here, a two-layered SiC porous burner with an external preheater and a radiation corridor, as shown in Fig. 1, was experimentally and numerically investigated for lean superadiabatic combustion of propane/air mixtures. The effects of the operating parameters for the porous burner such as fuel flow rate and equivalence ratio on the combustion characteristics and radiation efficiencies are discussed and the experimental and numerical results are compared.

2. Methods

2.1. Experiments

The superadiabatic radiant burner (SRB) with two porous sections (i.e., two-layer porous media), radiation rods embedded in the porous media and a preheater is considered for the present investigation since it is expected to provide superadiabatic flame temperature. A diagram of the experimental apparatus used in this study is shown in Fig. 2. The dimensions of the SRB are given in Table 1. It consists of a test SRB, a fuel–air mixture supply system, a ventilation system, thermocouples for measuring temperature distribution in the SRB, a gas analyzer for measuring nitrogen oxide (NO_x) and carbon monoxide (CO) emissions and a digital camera (Sony A65) for recording flame and radiation images.

Air (21% O_2/79% N_2 in volume, purity > 99.9%) and C_3H_8 (purity > 99.9999%) are supplied respectively to a preheater and to a mixing chamber using commercial mass flow controllers (Aera: 0–5 slm and MKS: 0–200 slm) with accuracy ±1.0% of full scale. The mass flow controllers are calibrated using a bubble meter. Air is preheated through the preheater and then is delivered to the mixing chamber. The preheater is a spiral fin tube with the inner diameter of 10.2 mm (stainless steel, SUS316L) and is located between the downstream end of the porous medium of the SRB and the radiation disks of the radiation rods. Thus, heat in exhaust gas is recovered to preheat fresh air in the preheater. The preheated air and fuel are mixed in the mixing chamber and are issued from the bottom of a distributor ($68 \times 68 \times 60$ mm^3) that is filled with stainless steel beads with an average bead diameter of 1.5 mm for obtaining uniform flow. The distributor is windowed to detect flashback using quartz. The preheated air–fuel mixture is fed into the porous medium of the SRB with uniform flow.

The test SRB is two-layered: a porous medium with fine silicon carbide (SiC) foam (PM1: 65 ppi, $68 \times 68 \times 40$ mm^3, Ultramet Inc.) upstream and the other porous medium with coarse SiC foam (PM2: 20 ppi, $68 \times 68 \times 40$ mm^3, Ultramet Inc.) downstream. The sides of porous media are surrounded by the heat-insulated case with thickness of 5 mm (SUS316L, $78 \times 78 \times 140$ mm^3). The preheated air–fuel mixture is ignited at the exhaust outlet of the

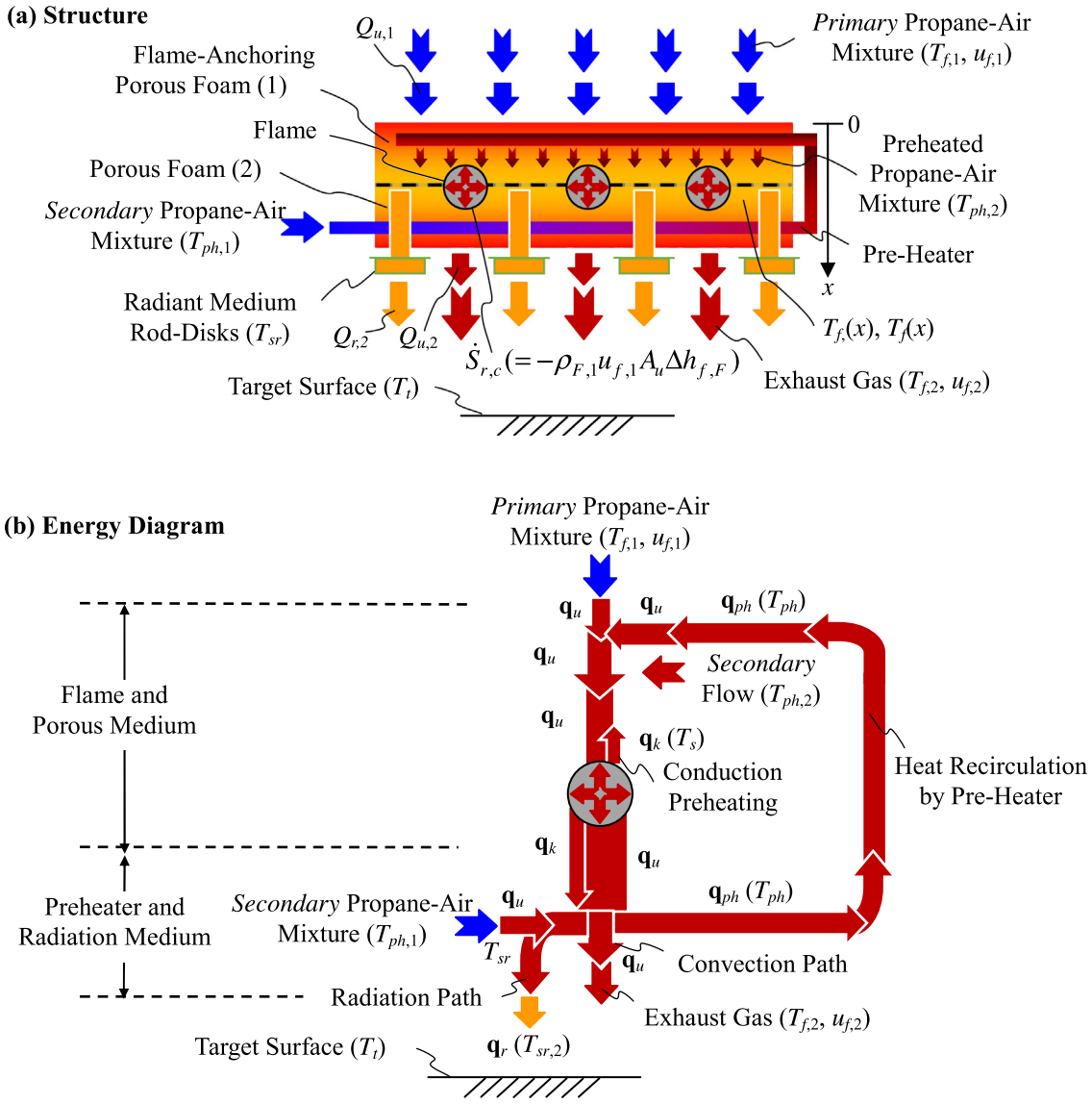

Fig. 1. (a) SRB schematic, (b) Energy flow diagram showing heat recirculation.

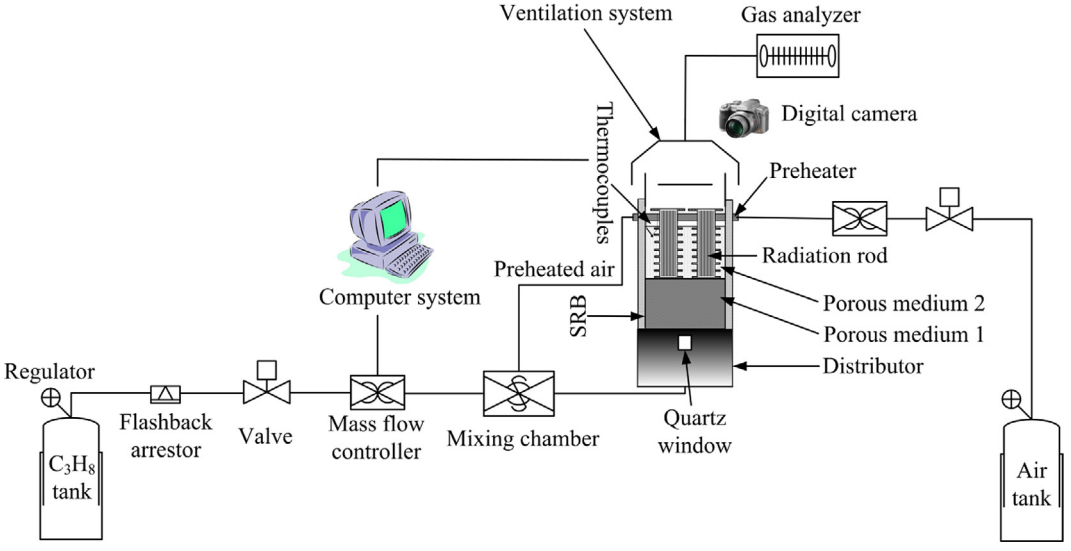

Fig. 2. Schematics of experimental apparatus.

Table 1
Specifications of SRB components.

Components	Parameters	Values
PM1	Material	Silicon Carbide (SiC)
	Length	40.0 mm
	Porosity	0.835
	Pore size	65 ppi
	Thermal conductivity	1.14 W/m-K
PM2	Material	SiC
	Length	40.0 mm
	Porosity	0.870
	Pore size	20 ppi
	Thermal conductivity	1.34 W/m-K
Radiation Rods	Material	SiC
	Stem diameter	14.0 mm
	Fin diameter	24.0 mm
	Fin thickness	1.5 mm
	Fin pitch	333 m^{-1}
	Disk diameter	32.0 mm
	Disk thickness	2.0 mm
	Length	90.0 mm
	Thermal conductivity	611/(*T*-115) W/cm-K [28]
Preheater (finned tube)	Material	Stainless steel (SUS316L)
	Inner diameter	10.2 mm
	Fin diameter	16.0 mm
	Fin thickness	1.0 mm
	Fin pitch	666 m^{-1}
	Tube thickness	0.5 mm
	Length	70.0 mm

burner by a torch-igniter. Once the mixture is ignited, the flame moves backward and is stabilized in the PM2 or on the interface between the PM1 and PM2. Heat from the flame is extracted through the fins around the stem of the embedded radiation rods (SiC), conducted through the stem and radiated at the radiation disk. Figs. 3 and 4 show the photographs of the assembled and disassembled SRB and the typical images of the radiating PM2 and disks, respectively.

R-type thermocouples with a bead diameter of 250 ± 20 μm and an accuracy of ± 0.25% are used to measure the temperature (T) distribution in the PM2. A stage on which the thermocouples are fixed can move through a hole that is drilled along the axial centerline, identifying the maximum flame temperature and its location. Measured temperature is corrected for radiative heat transfer between the bead surface and solid form by assuming a spherical bead and considering a quasi-steady energy balance with a constant Nusselt number (Nu) of 2.0 and constant emissivity of 0.3. Conduction along the wire leads of the thermocouples and the catalytic effect of the bead are neglected. Actually, it is challenging to correct gas temperature accurately, due to the complex interactions of flow, chemical reactions and inter-phase heat transfer in the PM2. An earlier study regarding the effects of varying solid temperature surrounding the bead, Nu and flow velocity over the bead on the corrected gas temperature shows that uncertainty for the corrected gas temperature is less than 5% in general [23]. Due to the imperfect contact between the thermocouple and the solid foam surface when the foam surface temperature is measured for the radiative calibration of gas temperature, however, the corrected gas temperature in the flame and post-flame zones may be underestimated. Thus, it should be noted that the actual gas temperature in the flame and post-flame zones of the PM2, including peak temperature, could be even higher than the corrected gas temperature that will be provided in Section 3. The preheated air temperature is measured using K-type thermocouples with a bead diameter of 250 ± 20 μm and an accuracy of ±0.75%. K-type thermocouples are also used to measure the radiation disk surface temperature and the exhaust gas temperature at the same axial location as the disk surface. The disk surface temperature and the exhaust gas temperature are obtained by averaging measurements at the same axial location but different points.

The combustion stability limits of fuel-lean C_3H_8/air flames in the SRB are measured by varying the fuel-equivalence ratio ϕ and the burner inlet velocity V that is defined as the total volume flow rate of the mixture divided by the cross-sectional area of the SRB. Propane has been chosen as fuel since it can be used in practical applications. Once a flame is stabilized in the PM2 as aforementioned, ϕ is set to a fixed value and then V is varied to find the combustion stability limits. Given ϕ, two combustion stability limits are observed in general: the flashback (i.e., low-stretch) limits at low Vs and the blow-off (i.e., high-stretch extinction) limits at high Vs. For some conditions no blow-off limits were obtained because of the limited capability of the present apparatus. The concentrations of NO_x and CO are also measured in the ventilation tube using a gas analyzer (Testo 350-XL) with an accuracy of 0.1–1.0 ppm: the probe is located on the center of the ventilation path. Final results are obtained by averaging measurements of 4–6 tests at each condition. Experimental uncertainties (95% confidence) for V and T are less than 5%. At NTP (298 ± 3 K) experiments were carried out for ϕ = 0.24–0.60 and V = 0.156–0.431 m/s.

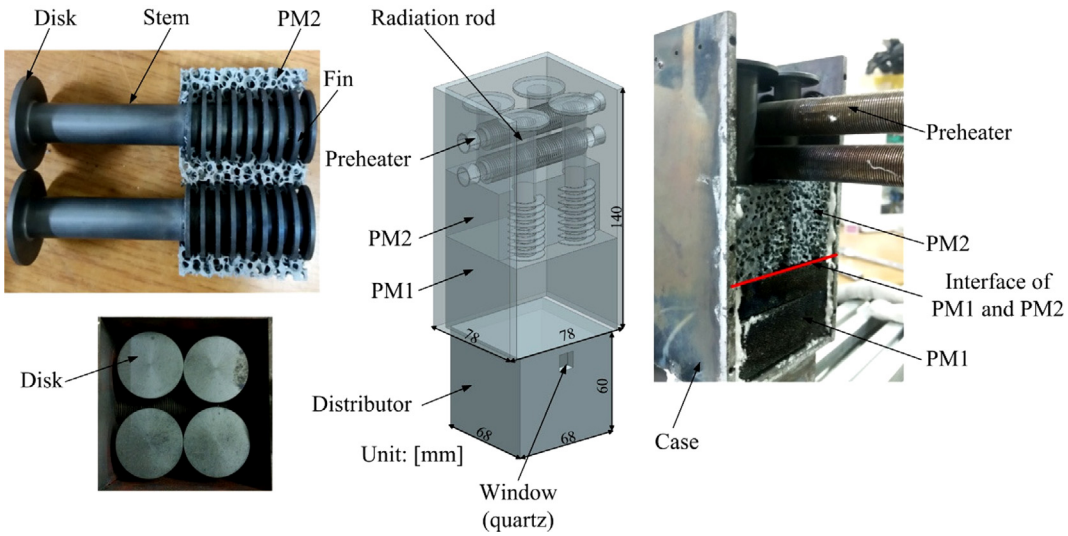

Fig. 3. Photographs of assembled and disassembled SRB.

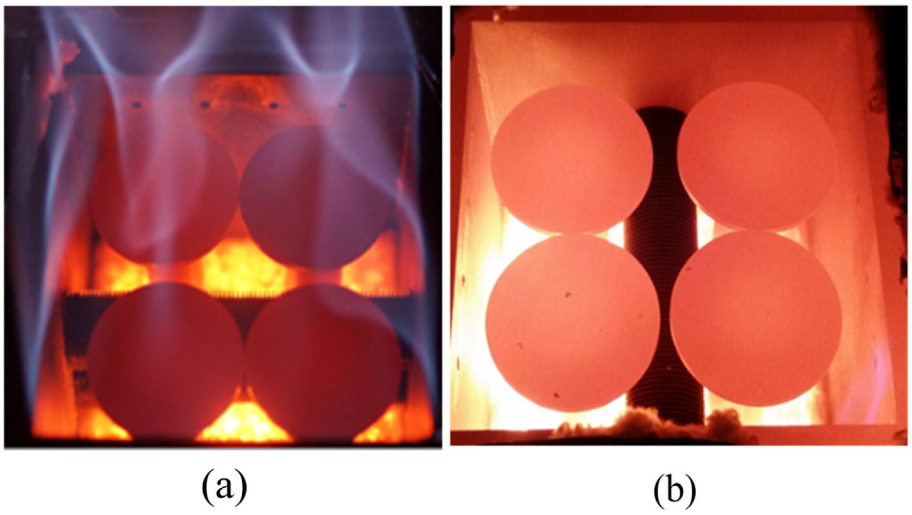

Fig. 4. Images of radiating PM2 and glowing radiation disks, (a) warming up condition, (b) steady condition.

2.2. Analyses

The radiant porous burner considered for a numerical analysis is shown in Fig. 5. The porous burner consists of two layers of porous media (PM1: SiC foam of fine pores and PM2: SiC foam of coarse pores) and a finned radiation rod (RR) with a radiating disk as solid SiC. Also a preheater downstream the burner (not shown in Fig. 5) is considered to recover the heat from the flue gas. The cold inlet air is heated in the preheater by the hot flue gas exiting from the porous burner. The preheated air is then mixed with the cold gaseous fuel flow in the upstream fine porous medium (PM1). The downstream coarse porous medium (PM2) serves as flame holder to stabilize the flame where the fins of the radiation rods are located.

The combustion heat is extracted by the fins of the radiation rods (RR) and transferred through the radiation rods by conduction to the radiating surface. The radiation rods provide a highly conducting path for the combustion heat directly from the flame to the radiating surface. It is assumed that the stem of radiation rod is coated with a low thermal conductivity material (thermal insulator) to reduce the heat loss to the surrounding flue gas being cooled by the preheater.

2.2.1. Porous burner

The porous burner shown in Fig. 5 is analyzed using non-equilibrium model in ANSYS Fluent [24]. Because of the geometric symmetry of the burner, only one eighth of the entire burner was considered for the numerical simulation. The energy conservation

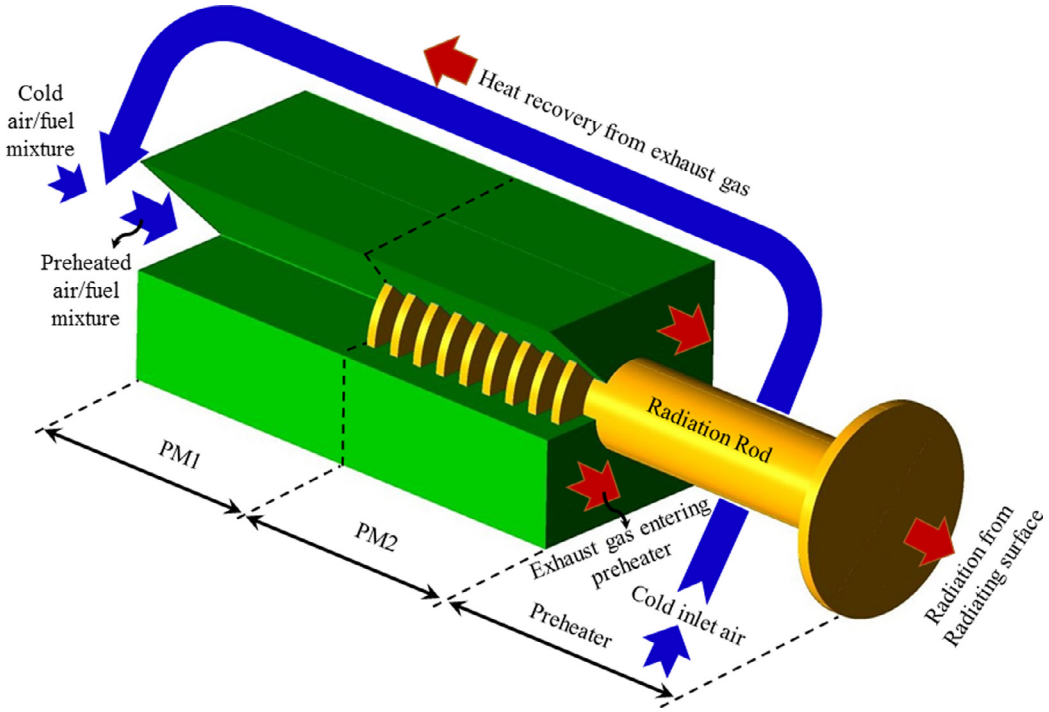

Fig. 5. Three-dimensional model of the porous superadiabatic radiant burner (SRB) used for the numerical simulations.

equations for gas and solid phases of the porous burner, species conservation of gas phases along with the momentum conservation equation are solved. The phases are assumed to be continuum. The energy conservation equation for the gas phase is given by

$$\frac{\partial}{\partial t}(\varepsilon\rho_g E_g) + \nabla\cdot[\vec{u}(\rho_g E_g + P_g)] = \nabla\cdot\left[\varepsilon k_g \nabla T_g - \left(\sum_i h_i J_i\right)\right] + h_{gs}\frac{A_{gs}}{V}(T_s - T_g) + S_g, \quad (1)$$

where the porosity, ε is defined as the ratio of the void volume to the total volume of the porous media. ρ_g is the gas density, and P_g, k_g, T_g and S_g are the gas pressure, thermal conductivity, temperature and source term due to reactions, respectively. E_g is the total energy of the gas phase given as

$$E_g = h_g - \frac{P_g}{\rho_g} + \frac{u^2}{2}, \quad (2)$$

where h_g is the sensible enthalpy defined for the ideal gas. The gas phase interacts with the solid phase only through the interstitial convection in which the specific area of the porous media is given by A_{gs}/V and the interstitial heat transfer coefficient is given by h_{gs}. The energy conservation equation of the solid phase of the porous burner is given by

$$\frac{\partial}{\partial t}[(1-\varepsilon)\rho_s E_s] = \nabla\cdot[(1-\varepsilon)k_s\nabla T_s] + h_{gs}\frac{A_{gs}}{V}(T_g - T_s), \quad (3)$$

where ρ_s is the solid phase density, E_s is the total energy of the solid phase and k_s and T_s are respectively the thermal conductivity and temperature of the solid phase. The conservation equations of the gas species are given by

$$\frac{\partial}{\partial t}(\rho_g Y_i) + \nabla\cdot(\rho_g \vec{u} Y_i) = -\nabla\cdot J_i + R_i, \quad (4)$$

where Y_i is the mass fraction and J_i is the diffusion flux of species i.

$$J_i = \left(-\rho D_{i,m}\nabla Y_i - D_{T,i}\frac{\nabla T}{T}\right), \quad (5)$$

where $D_{i,m}$ is the mass diffusion coefficient for species i in the mixture, and $D_{T,i}$ is the thermal diffusion coefficient.

Two-step combustion reaction of propane is considered for the reaction mechanisms.

$$C_3H_8 + \frac{7}{2}O_2 \rightarrow 3CO + 4H_2O \quad \text{for reaction} \quad r_1, \quad (6)$$

$$CO + \frac{1}{2}O_2 \rightarrow CO_2 \quad \text{for reaction} \quad r_2. \quad (7)$$

The rate constant for each reaction r, k_r is given by Arrhenius expression below

$$k_r = AT^{\beta}e^{-E_a/R_g T_g}. \quad (8)$$

The molar rate of creation or destruction of species i is given by

$$\bar{R}_{i,r} = (\nu''_{i,r} - \nu'_{i,r})\left(k_r\prod_{j=1}^{N}[C_{j,r}]^{(\eta''_{j,r}-\eta'_{j,r})}\right), \quad (9)$$

and

$$R_i = M_{w,i}\sum_{r=1}^{N_R}\bar{R}_{i,r}, \quad (10)$$

where N_R is the number of reactions that the species participate in. The coefficients of the reaction rates are given in Table 2.

The density of the gas flow is computed from the ideal gas law, in which the properties of the gas mixture are considered and is given by

$$\rho_g = \frac{P_g}{R_g T_g}. \quad (11)$$

The interstitial convective heat transfer is modeled by the volumetric Nusselt number [21] and is given by

$$\mathrm{Nu}_{D,p} = C\mathrm{Re}^m, \quad (12)$$

where C is 0.638 and 0.2 for upstream porous section (PM1) and downstream porous section (PM2), respectively. The corresponding m values are respectively, 0.5 and 0.96. Re is the Reynolds number of the gas flow in the porous media.

The effective thermal conductivity of the solid phase consists of the volume-averaged thermal conductivity and the radiative thermal conductivity of the solid phase and is given by [11]

$$k_{s,e} = (1-\varepsilon)k_s + \varepsilon k_{s,r}, \quad (13)$$

where the radiative thermal conductivity is given by

$$k_{s,r} = \frac{16\varepsilon_r\sigma_{SB}T_s^3}{3\sigma_e}. \quad (14)$$

The perfect mixing of the preheated air and fuel is assumed at the inlet of the burner. The equivalence ratio of the fuel/air mixture is given by

$$\phi = (\rho_{F,g}/\rho_g)/(\rho_{F,g}/\rho_g)_{stoich}. \quad (15)$$

It is also assumed that the porous burner exchanges the radiation heat at the inlet and outlet of the burner with surrounding surfaces at the preheated air temperature and the average preheater temperature, respectively.

2.2.2. Radiation rods and preheater

The radiation rod consists of a finned head, a straight stem and a radiating disk. The finned head is located near the interface of the two layers of the SiC foam. It is assumed that the gaps between the fins are filled with the porous material. Also the surface of the fins and radiation rod is subject to no-jump boundary conditions for the temperature.

The heat transfer analysis for the preheater is performed by using a User Defined Function (UDF) in ANSYS Fluent by assuming a fixed heat exchanger effectiveness of 0.5 for the preheater. The heat loss to the surroundings is modeled by considering a heat loss due to natural convection of ambient air. The surrounding temperature is assumed to be constant at 298 K. It is also assumed that a thermal insulator 5 mm thick with a thermal conductivity of 0.3 W/m^2 K is applied to the walls.

Table 2
Coefficients of Arrhenius reaction rates and the rate exponents in two-step propane reactions.

	Pre-exponential, A [1/s]		Activation energy, E_a [J/kmol]	Exponent, β
Reaction r_1	5.62e+09		1.256e+08	0.0
Reaction r_2	2.239e+12		1.7e+08	0.0
	C_3H_8	O_2	CO	H_2O
η, rate exponent in reaction r_1	0.1	1.65	0.0	0.0
	CO	O_2	CO_2	
η, rate exponent in reaction r_2	1	0.25	0	

3. Results and discussion

3.1. Combustion stability limits in SRB

The combustion stability limits have been extended remarkably (Fig. 6) using a preheater: the limit of ϕ from 0.43 with no preheater to 0.24. Compared with the previous alumina SRB [12], the limit of ϕ has also been extended from 0.28 to 0.24.

3.2. Superadiabaticity

Fig. 7 shows the gas temperature profiles for ϕ = 0.4, and different fuel flow rates. With increasing fuel flow rates, the peak temperature is enhanced, though its location does not seem to be sensitive to the flow rate within the current test range, showing the location at the peak temperature at 20 mm downstream from the interface. The tendency of the enhanced peak temperature with increasing fuel flow rates is observed since the flame is intensified with the increased amount of supplied fuel. The adiabatic flame temperature is computed using the NASA CEA (Chemical Equilibrium with Applications) code [25]. As shown in the figure the peak temperature for all the flames is higher than the AFT, which indicates the superadiabatic effects of the SRB. Considering heat losses to the surroundings even with thermal insulation under practical operating condition, this superadiabatic effect is remarkable. For example, the peak temperature is much higher than the actual AFT that is estimated when 10% heat losses are assumed. The AFT for the premixed C_3H_8/air flame of ϕ = 0.4 at NTP is 1305 K, indicating the difference between the AFT and the maximum peak temperature of 113 K (i.e., the maximum peak temperature 8.0% higher than the AFT). The results from the experimental measurements and numerical predictions are in a reasonably good agreement. As shown in Fig. 7, the maximum gas temperature occurs quite downstream (17 mm from the interface between the PM1 and PM2).

The contours of the gas and solid temperatures, heat of reaction, and fuel concentration shown in Fig. 8 clearly shows that the flame is stretched over the entire finned area and the gas temperature reaches its maximum at the location where all the fuel is consumed. The temperature of the surface of the 3-dimensional view of the radiation rod is also depicted in both figures in Fig. 8. In

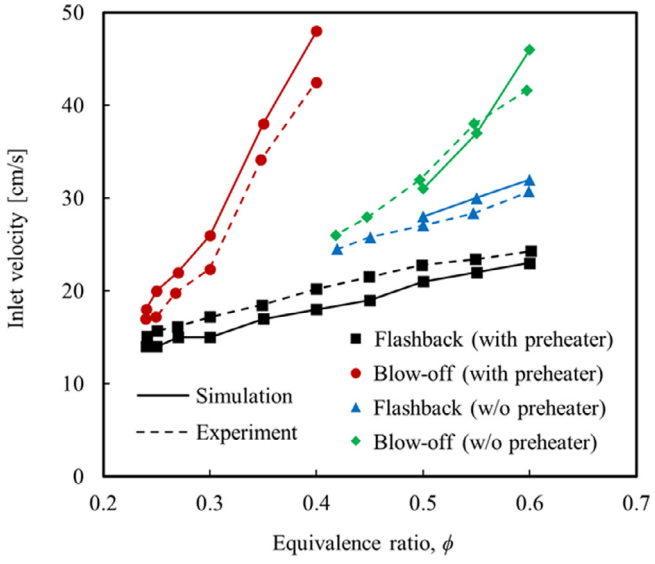

Fig. 6. Combustion stability limits on V–ϕ diagram for fuel-lean premixed C_3H_8/air flames in SRB at NTP.

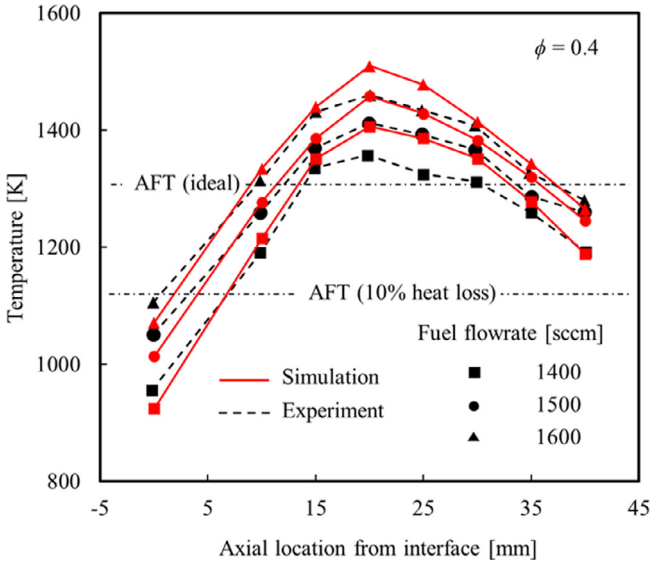

Fig. 7. Temperature distribution along axial centerline of PM2 for premixed C_3H_8/air flames of ϕ = 0.4 and various fuel flow rates.

the axial direction, the temperature of the radiation rod decreases due to the flux transferred to the radiating surface.

In addition to the superadiabatic effects in terms of the peak temperature in the PM2, temperature of radiating disk surfaces and the flue gas at the same axial location are also measured to observe if the former is higher than the latter. Fig. 9 shows the measured disk and flue gas temperature at the same axial location in terms of fuel flow rates for premixed C_3H_8/air flames of ϕ = 0.40 in the SRB at NTP. Both the disk and flue gas temperatures increase with increasing fuel flow rates because the burning in the PM2 is intensified. Due to the superadiabatic effects of the SRB, i.e., the preheating and the separate heat transfer through the radiation rods having high thermal conductivity, the radiating disk surface temperature is higher than the flue gas temperature for all the tests which was reported as a temperature reversal [10]. The temperature reversal is the direct result of using conduction-radiation rod-disk (radiation corridors) through which the heat is directed from the flame to the target. These corridors are absent in conventional radiant porous burners, so the temperature of radiating solid matrix surface is always lower that the flue gas. This solid matrix temperature drops sharply due to radiation heat transfer at the exit [26,27]. It is also shown that the numerical simulations predict a higher flue gas temperature backside of the disk which can be attributed to the additional heat losses which might happen in the experiments.

3.3. Emissions and efficiencies

The emissions of NO_x from the exhaust gas as a function of fuel flow rates for premixed C_3H_8/air flames of various fuel-equivalence ratios (ϕ = 0.3–0.6) in the SRB at NTP are given in Fig. 10. All the NO_x concentrations in the figure are corrected to 15% O_2. For a given ϕ, the NO_x concentration increases with increasing fuel flow rates in general, which is observed since the peak temperature that is enhanced due to the intensified burning strongly affects NO_x emissions via a thermal mechanism. For a fixed fuel flow rate, the NO_x concentration also increases with increasing ϕ in general, again due to the thermal NO_x mechanism. Compared with the previous alumina SRB [12], however, NO_x emissions are somewhat enhanced, though this level of NO_x emissions, which is well below the general standards, e.g., 70 ppm for commercial burners by

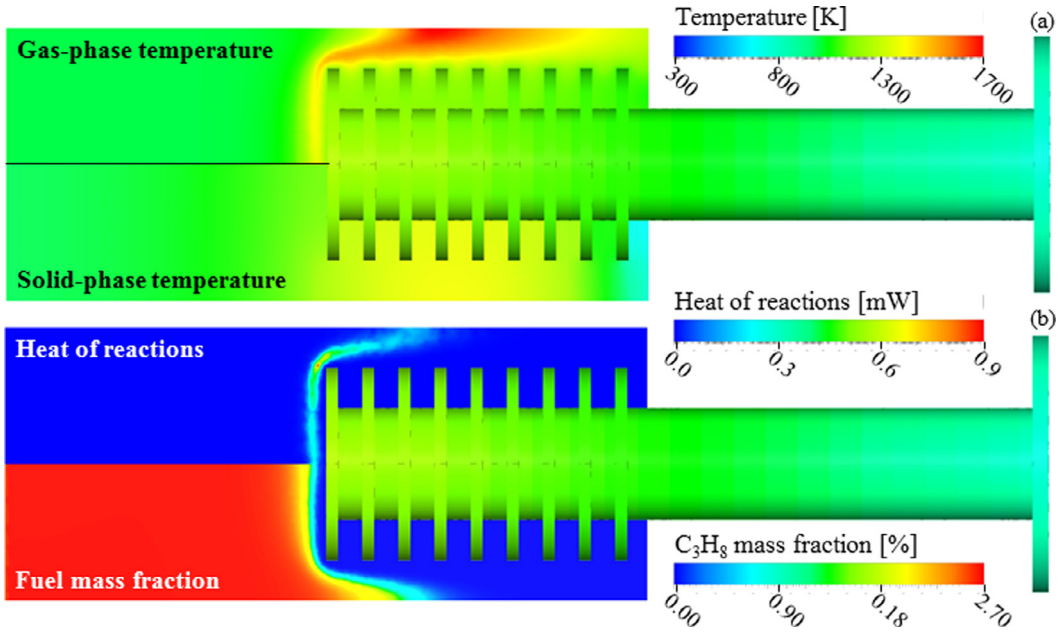

Fig. 8. Contours of the (a) gas and solid temperatures, (b) heat of reaction, and fuel concentration for $\phi = 0.40$. The contour of the surface temperature of the radiation rod is also depicted.

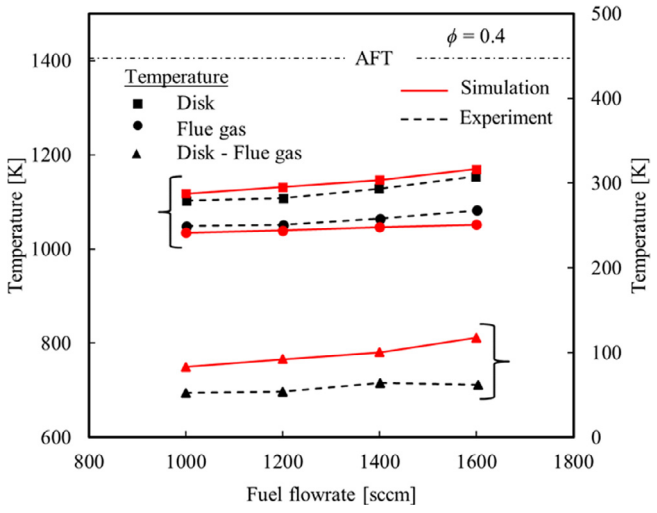

Fig. 9. Temperature of the disk and flue gas for different fuel flow rates. Premixed C_3H_8/air flames at equivalence ratio of $\phi = 0.40$ in SRB at NTP.

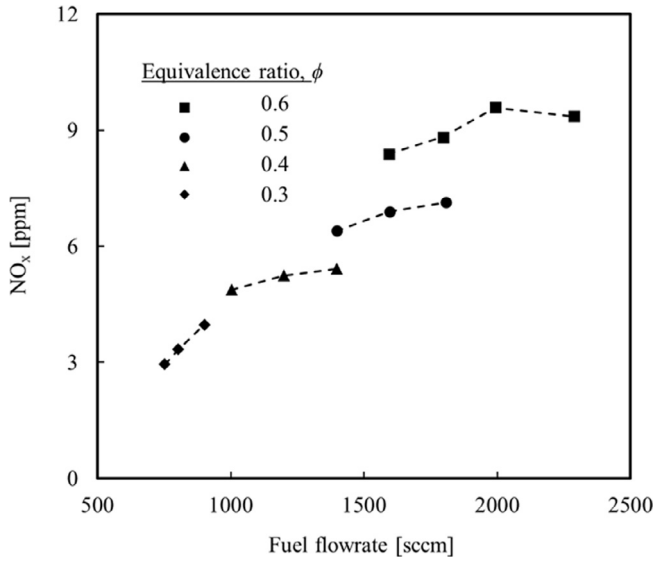

Fig. 10. NO_x emissions from exhaust gas as a function of fuel flow rates for premixed C_3H_8/air flames of various fuel-equivalence ratios in SRB at NTP.

Southern California Emission Standards, indicates that the SRB is acceptable for practical applications and the emission performance is even better than the conventional porous radiant burners for most operating conditions [19].

Fig. 11 shows CO emissions from the exhaust gas as a function of fuel flow rates for premixed C_3H_8/air flames of various fuel-equivalence ratios ($\phi = 0.3$–0.6) in the SRB at NTP. In general, the CO concentration is below 25 ppm, except for very fuel-lean and low fuel flow rate conditions. This level of CO emissions indicates that the SRB is acceptable for practical applications and the emission performance is even better than the conventional porous radiant burners for most operating conditions [19]. At very fuel-lean conditions, CO emissions rapidly increase with decreasing fuel flow rates. This tendency is observed since the flame temperature is very low and thus oxidation (to carbon dioxide, CO_2) rates are reduced. At moderate to high fuel flow rates (>1400 sccm) CO emissions do not seem to be sensitive to both the fuel flow rate and ϕ, though for a fixed fuel flow rate the CO concentration somewhat decreases with increasing ϕ.

The radiation efficiencies of the radiation disk in the present SRB are estimated and given in Fig. 12, which shows radiation efficiencies (η_r) as a function of fuel flow rates (and also ϕ) for premixed C_3H_8/air flames in the SRB at NTP. The radiation efficiency (η_r) is the ratio of the radiated energy from the radiating disk and the combustion heat. As shown in the figure, η_r increases with increasing ϕ (and fuel flow rates) since the flame temperature increases so that more heat is extracted through the radiation fins and conducted to the radiation disk surface. As expected, η_r of the SRB has been enhanced due to the preheater, i.e., the external heat recirculation, showing the maximum η_r of 37% in the present study.

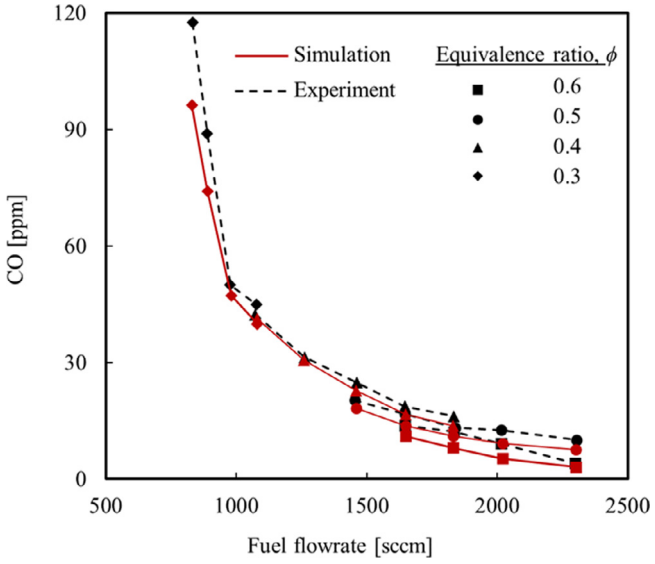

Fig. 11. CO emissions from exhaust gas as function of fuel flow rates for premixed C_3H_8/air flames of various fuel-equivalence ratios in SRB at NTP.

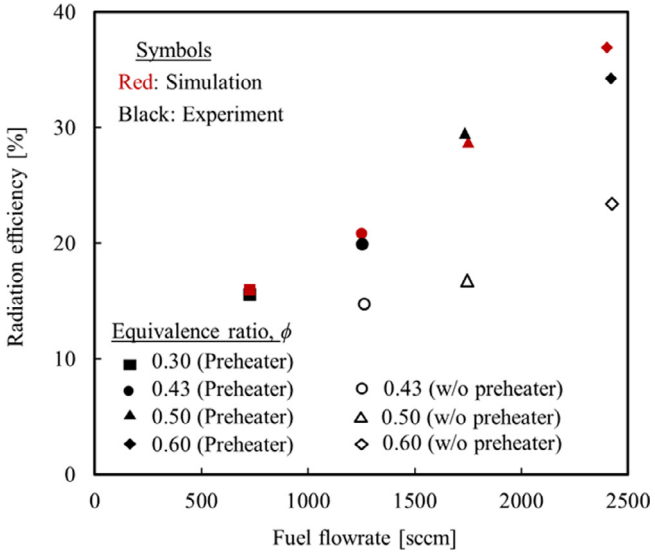

Fig. 12. Radiation efficiencies of disk as a function of fuel-equivalence ratios (and fuel flow rates) for premixed C_3H_8/air flames in SRB at NTP.

4. Conclusions

To increase the radiant efficiency, the exiting flue gas enthalpy flow has to be reduced, requiring the flue gas exit at temperature below the radiating surface. To achieve this, two heat-management steps were added to the superadiabatic porous burner. One is a conduction conduit that directly and effectively transfer heat from the flame location to the radiating disks. The other is the preheater that heats the secondary air and cools the flue gas. With these we have recorded flue gas exiting over 50 K below the radiating disks, and radiation efficiency as high as 37% with a two-layered porous burner (propane) made of SiC foams. The multiscale thermal nonequilibria (internal heat recirculation, local superadiabatic combustion and external preheating), and effective SiC rod heat routing to radiating disks are responsible for this reversed temperature (higher solid temperature than exhaust gas) leading to such a record efficiency. The lean flammability limit was extended to 0.24 equivalence ratio. The emissions of NO_x and CO are well below the general standards, indicating that the SRB is acceptable for practical applications. The predictions show excellent agreement with the measurements over wide ranges of fuel flow rate and equivalence ratios.

Acknowledgement

This research was supported by *Basic Science Research Program* through the National Research Foundation of Korea (NRF) funded by the Ministry of Education (No. 2013R1A1A2006403). M. Kaviany is grateful for support through the *Propane Challenge Fund* of the Propane Education and Research Council.

References

[1] D.K. Min, H.D. Shin, Laminar premixed flame stabilized inside a honeycomb ceramic, Int. J. Heat Mass Transfer 34 (2) (1991) 341–356.
[2] K. Hanamura, R. Echigo, S.A. Zhdanok, Superadiabatic combustion in a porous medium, Int. J. Heat Mass Transfer 36 (13) (1993) 3201–3209.
[3] J.R. Howell, M.J. Hall, J.L. Ellzey, Combustion of hydrocarbon fuels within porous inert media, Prog. Energy Combust. Sci. 22 (2) (1996) 121–145.
[4] M. Sahraoui, M. Kaviany, Direct simulation vs volume-averaged treatment of adiabatic, premixed flame in a porous medium, Int. J. Heat Mass Transfer 37 (18) (1994) 2817–2834.
[5] A.A.M. Oliveira, M. Kaviany, Nonequilibrium in the transport of heat and reactants in combustion in porous media, Prog. Energy Combust. Sci. 27 (5) (2001) 523–545.
[6] C. Park, M. Kaviany, Combustion-Thermoelectric Tube, ASME J. Heat Transfer 122 (2000) 721–729.
[7] C. Park, M. Kaviany, Evaporation-combustion affected by in-cylinder, reciprocating porous-regenerator, ASME J. Heat Transfer 124 (2002) 184–194.
[8] M.T. Smucker, J.L. Ellzey, Computational and experimental study of a two-section porous burner, Combust. Sci. Technol. 176 (8) (2004) 1171–1189.
[9] V. Bubnovich, M. Toledo, L. Henríquez, C. Rosas, J. Romero, Flame stabilization between two beds of alumina balls in a porous burner, Appl. Therm. Eng. 30 (2–3) (2010) 92–95.
[10] V. Vandadi, C. Park, M. Kaviany, Superadiabatic radiant porous burner with preheater and radiation corridors, Int. J. Heat Mass Transfer 64 (2013) 680–688.
[11] V. Vandadi, C. Park, 3-Dimensional numerical simulation of superadiabatic radiant porous burner with enhanced heat recirculation, Energy 115 (2016) 896–903.
[12] H. Wu, Y.J. Kim, V. Vandadi, C. Park, M. Kaviany, O.C. Kwon, Experiment on superadiabatic radiant burner with augmented preheating, Appl. Energy 156 (2015) 390–397.
[13] S. Wood, A.T. Harris, Porous burners for lean-burn applications, Prog. Energy Combust. Sci. 34 (5) (2008) 667–684.
[14] Y. Kotani, H. Behbahani, T. Takeno, An excess enthalpy flame combustor for extended flow ranges, in: Twentieth Symposium (International) on Combustion, The Combustion Institute, 1984, pp. 2025–2033.
[15] I. Glassman, Combustion, 3rd ed., Academic Press, San Diego, 1996.
[16] T. Takeno, K. Sato, K. Hase, A theoretical study on an excess enthalpy flame, Symp. (Int.) Combust. 18 (1) (1981) 465–472.
[17] K. Hanamura, R. Echigo, An analysis of flame stabilization mechanism in radiation burners, Wärme-und Stoffübertragung 26 (6) (1991) 377–383.
[18] R.C. Catapan, A.A.M. Oliveira, M. Costa, Non-uniform velocity profile mechanism for flame stabilization in a porous radiant burner, Exp. Thermal Fluid Sci. 35 (1) (2011) 172–179.
[19] V. Khanna, R. Goel, J.L. Ellzey, Measurements of emissions and radiation for methane combustion within a porous medium burner, Combust. Sci. Technol. 99 (1–3) (1994) 133–142.
[20] F. Durst, D. Trimis, Combustion by free flames versus combustion reactors, Clean Air 3 (2002) 1–20.
[21] L.B. Younis, R. Viskanta, Experimental determination of the volumetric heat transfer coefficient between stream of air and ceramic foam, Int. J. Heat Mass Transfer 36 (6) (1993) 1425–1434.
[22] P.-F. Hsu, W.D. Evans, J.R. Howell, Experimental and numerical study of premixed combustion within nonhomogeneous porous ceramics, Combust. Sci. Technol. 90 (1–4) (1993) 149–172.
[23] C. Zheng, L. Cheng, A. Saveliev, Z. Luo, K. Cen, Gas and solid phase temperature measurements of porous media combustion, Proc. Combust. Inst. 33 (2) (2011) 3301–3308.
[24] ANSYS® Academic Research, Release 16.2., in.
[25] S. Gordon, S.B.J. McBride, Computer program for calculation of complex chemical equilibrium compositions and applications, NASA Report RP-1311-P2, Cleveland, OH, USA, 1996.

[26] A.J. Barra, G. Diepvens, J.L. Ellzey, M.R. Henneke, Numerical study of the effects of material properties on flame stabilization in a porous burner, Combust. Flame 134 (4) (2003) 369–379.
[27] A.J. Barra, J.L. Ellzey, Heat recirculation and heat transfer in porous burners, Combust. Flame 137 (1–2) (2004) 230–241.
[28] O. Nilsson, H. Mehling, R. Horn, J. Fricke, R. Hofmann, S.G. Müller, R. Eckstein, D. Hofmann, Determination of the thermal diffusivity and conductivity of monocrystalline silicon carbide (300–2300 K), High Temp. High Pressures 29 (1) (1997) 73–79.
[29] V. Vandadi, C. Park, 3-Dimensional numerical simulation of superadiabatic radiant porous burner with enhanced heat recirculation, Energy 115, Part 1 (2016) 896–903.